Journal of Materials Chemistry A

ROYAL SOCIETY OF CHEMISTRY

PAPER

View Article Online
View Journal

Cite this: DOI: 10.1039/d5ta04830c

Controlled distribution of both Pt nanoparticles and ionomer in self-supported nanoporous carbon scaffolds significantly enhances oxygen reduction kinetics and stability

Marwa Atwa, [abc] Shicheng Xu,[c] Xiaoan Li,[a] Samuel Dull,[d] Zhaoxuan Wang,[e] Haoyang Yu,[f] Rui Tang,[g] Timothy Goh,[e] Yunha Jung,[e] Mehrdad Kiani,[e] Markus Lid,[ch] Hirotomo Nishihara, [g] Fritz B. Prinz[ceh] and Viola Birss *[a]

We have developed a family of binder-free, bimodal, ball-and-stick carbon scaffolds (BCS) to overcome the poisoning of Pt nanoparticles (NPs) by Nafion ionomer in polymer exchange membrane (PEM) fuel cell cathodes. The BCS design features sub-micron-sized spheres containing 3D interconnected mesopores (~12 nm) that house only the Pt NPs. Nafion resides only on the outer sphere surfaces, size-screened out from direct contact with the NPs, as verified by the unique hydrogen adsorption (HUPD) profile observed. Proton transport is facilitated along wet hydrophilic mesopore surfaces at 100% relative humidity (RH), enabled by a rich density of oxygen-functionalities, confirmed by temperature-programmed desorption and the RH dependence of the Pt electrochemically active surface area (ECSA). Notably, an exceptionally high ECSA of Pt NPs (~100 m^2 g_{Pt}^{-1}) is achieved in a membrane-electrode assembly (MEA), even without any Nafion in the cathode. The Pt/BCS catalyst layers exhibit enhanced oxygen reduction reaction (ORR) kinetics, achieving very high activity (0.58 ± 0.1 A mg_{Pt}^{-1}) and durability in MEAs. These results establish a direct link between ionomer poisoning of Pt and ORR activity while also demonstrating the effectiveness of combining tailored carbon scaffolds and oxygen-rich surfaces to achieve ultra-high electrocatalytic performance.

Received 14th June 2025
Accepted 4th August 2025

DOI: 10.1039/d5ta04830c

rsc.li/materials-a

Introduction

Intense worldwide efforts are being focused on decreasing the world's reliance on fossil fuels and reaching a sustainable energy future, with a common vision being the generation of green hydrogen as a net-zero fuel by water electrolysis powered by renewable energy sources. Given this developing paradigm, hydrogen-based fuel cells are a natural fit, considering their high energy conversion efficiency and clean products (water). Proton exchange membrane fuel cells (PEMFCs) are currently the front-running option, due to their high power density, fast start-up,[1] and near room temperature operation, making them ideal also for transportation applications.[2,3] PEMFCs currently still rely primarily on Pt to catalyze both the hydrogen oxidation and oxygen reduction (ORR) reactions, with Pt typically employed in nanoparticle (NP) form in order to maximize the surface to area ratio and thus lower cost. Pt NPs provide the best combination of activity and stability, especially for the sluggish ORR,[4] which is the performance-limiting reaction that is the target of the vast majority of current PEMFC electrocatalyst research and development.

In present-day PEMFCs, both the anode and cathode catalyst layers are constructed from inks containing electronically conducting carbon powders that support the Pt NPs and are mixed with an ionically conducting perfluorosulfonic acid proton-conducting ionomer, such as Nafion. In an ideal catalyst layer, the carbon particles are fully interconnected to promote high electronic conductivity, with the ionomer, deposited as a continuous phase on or near the catalytic NPs, facilitating the conduction of protons to/from the active sites during the electrocatalytic reactions.[5] Furthermore, inter-connected pores must also be present throughout the catalysts layers to serve as conduits for facile gas transport.[6]

[a]Department of Chemistry, University of Calgary, 2500 University Dr NW, Calgary, AB, T2N 1N4, Canada. E-mail: birss@ucalgary.ca
[b]Department of Chemistry, Suez Canal University, El Salam District, Ismailia, 41522, Egypt
[c]Department of Mechanical Engineering, Stanford University, Building 530, 440 Escondido Mall, Stanford, CA, 94305, USA
[d]Department of Chemical Engineering, Stanford University, 443 Via Ortega, Stanford, CA, 94305, USA
[e]Department of Material Science and Engineering, Stanford University, 496 Lomita Mall, Stanford, CA, 94305, USA
[f]NanoFAB Centre, University of Alberta, Edmonton, AB, T6G 2V4, Canada
[g]Advanced Institute for Materials Research (WPI-AIMR)/Institute of Multidisciplinary Research for Advanced Materials, Tohoku University, 2-1-1 Katahira, Aoba-ku, Sendai, 980-8577, Japan
[h]Department of Mechanical and Industrial Engineering, Norwegian University of Science and Technology, Høgskoleringen 1, Trondheim, 7491, Norway

This highly complex 3-dimensional structure is the key to achieving increasingly stringent PEMFC performance and durability metrics, with the majority of the critical parameters defined by the microstructure and surface properties of the carbon support. For example, when using ink-deposition methods, the channels between carbon particles are tortuous and uncontrolled, and when using microporous carbons (*e.g.*, carbon black), the Pt NPs must be supported on the outer surface of the carbon particles, thus being prone to agglomeration and dissolution. To overcome these challenges, efforts have increasingly moved towards the use of mesoporous carbons, including Ketjen Black, allowing the Pt NPs to be stabilized by housing them inside the pores, while also enhancing gas transport.[7,8] In addition, many studies have been focused on developing graphene nanocages or nanopockets to encapsulate the Pt NPs and hinder Pt agglomeration.[9–12] While these nanocages successfully enhance Pt stability, they have been found to hinder gas accessibility and transport, causing a drop in performance of the fuel cell device.

Another complicating issue that is known to compromise PEMFC performance, especially the ORR activity at the cathode, is related to the ionomer phase. While Nafion is considered essential for proton transport during the ORR and also serves as the binder to hold the Pt/C particles together, several studies have found that the sulfonate group terminating the Nafion side chains can specifically adsorb and even poison Pt surfaces.[13–20] This is especially true at the positive potential of the cathode, causing a significant decrease (by 2–4 times) in the already sluggish ORR kinetics.[13–16] Also, the thin Nafion film that often coats the Pt NPs leads to a gas–ionomer interface resistance for the mass transport of oxygen.[17] The Nafion-to-carbon ratio must therefore be carefully optimized to balance the needed proton conductivity with these undesirable oxygen mass transport resistance and catalyst poisoning effects, with these efforts depending on the type of ionomer, catalyst, and carbon support employed. This unavoidably leads to performance compromises, with a step-change forward remaining difficult due to the uncertainty and variability in the distribution of each catalyst layer component and their local environments within conventional PEMFC cathodes.

Efforts to overcome the challenges associated with Nafion poisoning of Pt have included the development of ionomer-free electrodes, such as the nanostructured thin films pioneered by 3M,[21] in which proton transport occurs along the surface of an inter-connected Pt thin film with assistance from water vapor, without the need for any ionomer.[22] However, these Pt thin films usually have quite low electrochemical surface areas (ECSA, 10–20 $m^2\ g_{Pt}^{-1}$), causing significant voltage losses at high current densities.[23] Another strategy has been to modify the pore size, inter-particle tortuosity, and wettability of carbon powder supports. For example, Yarlagadda and coworkers[24] found that mesoporous carbons (4–7 nm pores) with a high surface area and pore volume can boost the Pt mass activity for the ORR to 0.36 A mg_{Pt}^{-1} by housing the Pt NPs inside the carbon mesopores, a short distance away from the ionomer. However, these mesoporous carbon powders require substantial optimization of the ink formulation and of the methods used to spray ink onto the membrane or gas diffusion layer (GDL).[25,26]

The effect of the carbon support in determining the catalyst–ionomer interactions and therefore the catalytic activity was also studied by Kabir *et al.*[27] and our group.[28] As a host to both the catalyst and ionomer, the carbon support clearly plays a critical role in establishing the specific environment for the catalyst and ionomer and thus influences the interactions between them. Even so, traditional carbon supports generally offer only uncontrolled and disordered environments for housing the catalyst and ionomer, with the carbon particle size, pore size, and surface wettability heavily influencing where the Pt NPs and ionomer ultimately reside.

Here, we have developed a revolutionary cathode catalyst layer microstructure, namely an organized, self-supported, bimodal carbon scaffold (BCS) containing two scales of porosity, where the Pt catalyst is located in a highly organized and controllable microenvironment that is free of ionomer but is embedded within a catalyst layer that still contains sufficient ionomer. This seemingly self-contradictory objective has been achieved here by the construction of a 'ball and stick' bimodal carbon scaffold (BCS). The BCS contains a set of fully interconnected close-packed 12 nm primary pores that are inside larger spheres that exclusively house the Pt NPs, introduced *via* atomic layer deposition (ALD), with the 12 nm pores being too small for Nafion to penetrate. ALD enables atomic-scale control of the thickness and uniformity of the Pt deposit, offering exceptional conformality, even on complex surfaces, which is highly beneficial for catalyst decoration of the BCS substrates. Furthermore, ALD minimizes defects and contamination while exhibiting excellent reproducibility and scalability for both research applications and for the construction of larger scale devices for industrial applications.[29] In addition to the 12 nm pores within the BCS, a second set of larger secondary pores is present between the spheres, allowing Nafion to infiltrate and coat the outer surface of the spheres while also promoting fast gas transport. This equates to a bimodal structure and function, with proton transport to the Pt NPs occurring during the ORR through a potential water layer inside the 12 nm pores, while Nafion ionically interconnects the spheres and allows protons to transport across the full thickness of the BCS catalyst layer.

When tested in a membrane electrode assembly (MEA), the best-performing Pt/Nafion/BCS catalyst layer is shown to exhibit an exemplary ORR mass activity of 0.58 A mg_{Pt}^{-1} at 0.9 V that exceeds DOE targets, as well as a specific activity of 0.45 mA cm_{Pt}^{-2} at 0.9 V that is competitive with the best yet reported for pure Pt/C systems. Furthermore, the Pt/Nafion/BCS-based MEA demonstrates excellent stability after 10 000 cycles of accelerated durability testing (ADT), even displaying degradation reversal under certain ADT conditions. Together with these outstanding performance metrics, the BCS has provided an unprecedented avenue for investigating the ionomer-free catalytic activity of Pt nanoparticles.

Experimental details

BCS synthesis

The synthesis of the BCS films was outlined in detail in our previous work.[30–33] In particular, BCS films with a nominal pore

size of 12 nm and a bimodal porous structure were prepared using the same procedure reported for NCS membranes prepared with a monodisperse pore size, such as 85 nm (*e.g.*, NCS85).[30] Briefly, 0.1 g of mesophase pitch (MP, Momentum Materials Corp.), 0.2 g of *n*-butanol, and 5.0 g of 10% polyvinyl alcohol (PVA, Alfa Aesar, 86–89% hydrolyzed) were ball-milled together, making a uniform MP/PVA ink. Then, a colloidal silica suspension containing 0.5 g silica (Ludox HS-40, average particle sizes of 12 nm) was added to 1.0 g of a 1,3-propanediol (PD):water (mass ratio 1 : 1) to produce a silica suspension. Next, the silica suspension was added to the MP/PVA ink and then ball-milled to obtain the MP/PVA/PD/silica ink (or slurry), which was then degassed for 15 min to remove any bubbles.

The slurry was then tape-casted onto glass with a 0.010-inch gap between the doctor blade and the substrate. After drying overnight, a pristine composite MP/PVA/PD/silica film was obtained. These films were imprinted in an alumina tubular furnace at 400 °C for two hours in nitrogen, then heated at 900 °C for two hours in nitrogen to achieve carbonization. Finally, the carbonized films were brought to room temperature and soaked in 3 M NaOH at 80 °C for two days to remove the silica template, followed by successive washing with 1 M HCl, deionized water, and then drying at 80 °C overnight.

Pt/BCS and Pt/NCS synthesis *via* atomic layer deposition (ALD)

Trimethyl(methylcyclopentadienyl) platinum(IV) ($MeCpPtMe_3$, Strem Chemicals) was used as the Pt ALD precursor, with air used as the oxidant. Pt ALD was conducted at a reactor temperature of 190 °C, and the Pt precursor was heated at 78 °C. The exposure time for both the Pt precursor and air was optimized, being 9 s and 5 s, respectively. Argon was used as the inert gas to remove any unreacted precursor. The inert gas purge time after Pt precursor exposure was 100 s and the purge time after air exposure was 50 s.

Nafion loading method

For Nafion loading into the Pt/BCS or Pt/NCS films, the films were placed on a gas diffusion layer/microporous layer (GDL/MPL) assembly (Freudenberg H23C8, Fuel Cell Store) and *ca.* 60 μl of 4 wt% of Nafion solution D2021 in isopropyl alcohol was drop-casted onto the Pt-loaded film to produce the gas diffusion electrodes (GDEs).

Material characterization

Nitrogen gas sorption analysis was performed using a 3Flex Version 3.01 analyzer (Alberta Sulfur Research Ltd). The specific surface area and porosity of the BCS samples were measured at 77 K after prior degassing at 150 °C for 4 hours.

Advanced temperature-programmed desorption (TPD) was performed using an in-house high vacuum apparatus.[34] Samples were heated to ultra-high temperatures of 1800 °C to fully decompose the oxygen-functional groups on the BCS surface and to convert the H-terminated edge sites to H_2O, CO, CO_2, and H_2 gases. The quantification of the evolved gases thus enabled the precise bulk analysis of the H and O contents in the samples.

X-ray photoelectron spectroscopy was performed using a PHI VersaProbe 1 with Al(Kα) radiation of 1486 eV. Field emission scanning electron microscopy (FESEM) analysis was carried out using a Zeiss Sigma VP at an accelerating voltage of 8 kV. Separately, spatial maps for platinum were collected *via* energy dispersive X-ray spectroscopy (EDS) on an FEI Quanta 250 FEG with a Bruker Quantax attachment.

Scanning/transmission electron microscopy (S/TEM) imaging was performed on a JEOL JEM-ARM200cFS/TEM instrument, equipped with a cold Field-Emission Gun (cFEG) and a probe Cs corrector, at an accelerating voltage of 200 kV. The STEM images (HAADF, BF and BEI modes) with EDX mapping were collected using the following experimental conditions: probe size 4c, condenser lens aperture 30 μm, scan speed 40 μs per pixel, and camera length 8 cm. Samples were examined either as drop-casted ethanol-based suspensions of the BCS or NCS powder on Cu grids or as 100 nm microtomed cross-sectional slices of the Pt/BCS films and MEA catalyst layers.

Cyclic voltammetry in aqueous solutions was carried out with a Bio-Logic SP-300 potentiostat using a 3-electrode cell containing deaerated 0.5 M H_2SO_4, a platinized Pt mesh as the counter electrode, and a reversible hydrogen (RHE) reference electrode. Generally, a piece of the BCS or Pt/BCS film (*ca.* 1 cm^2) was sandwiched between two pieces of glass coated gold slides, where a small circular hole was cut into one of them to expose a 0.8 cm^2 area of the film to the solution to serve as the working electrode.

The ECSA of Pt in the Pt/NCS films was determined from the charge associated with the hydrogen underpotential deposition (HUPD) region. A charge density of 210 μC cm_{Pt}^{-2} is assumed to correspond to a full monolayer of hydrogen adsorbed on 1 cm^2 of Pt surface, which is the standard value used in the literature.[35] The ECSA (in $m^2\ g_{Pt}^{-1}$) was calculated using the following equation:

$$\text{ECSA} = \text{charge in HUPD peaks (C cm}^{-2})/[210 \times 10^{-6}\ (\text{C cm}_{\text{Pt}}^{-2}) \times 10 \times \text{Pt mass loading (mg}_{\text{Pt}}\ \text{cm}^{-2})]$$

The Wilhelmy plate method was used to measure the water contact angle of BCS under ambient conditions (25 °C and 0.1 MPa).[36] DI water was gradually added onto 1 × 2 cm^2 pieces of BCS in a Petri dish, while a Canon EOS Rebel SL2 camera recorded the droplet shapes at 25 frames per second. Equilibrium contact angles were then measured using ImageJ.

MEA construction and testing

After ALD of platinum, the Pt loading of the Pt*x*/BCS and Pt10/NCS85 films was measured using X-ray fluorescence (XRF) using an AMETEK Spectro Xepos HE. For single cell tests, each film was then placed on a carbon paper gas diffusion layer (Freudenberg H23C8, Fuel Cell Store) onto which a 4 wt% isopropanol-based solution of Nafion D2021 was drop casted and left to air-dry. The ionomer : carbon ratio was estimated to

be ~4, based on the volume of the Nafion solution D2021 added to the isopropyl alcohol. However, this ratio is just an estimate, as during drop-casting, some of the ionomer solution went into the MPL/GDL. After air drying, the cathode GDE was hot pressed onto a commercial anode-coated membrane (ACM), where the film thickness was 18 μm, the anode catalyst layer thickness was about 5 μm, and the Pt/C anode had a Pt loading of 0.1 mg_{Pt} cm^{-2}, all at 120 °C and at 500 lbf per cm^2. The anode active area was kept constant during all MEA measurements at 5 cm^2, while the cathode area was 1.6 ± 0.4 cm^2.

The resulting gas diffusion electrode (GDE) was then assembled with a commercial anode-coated membrane (ACM) (18 μm thick, anode Pt loading of 0.1 mg_{Pt} cm^{-2}) and hot pressed at 120 °C and 500 lbf per cm^2. These membrane electrode assemblies (MEA) were then assembled with Freudenberg H23C8 gas diffusion layers and compressed to 4 bar between graphite serpentine flow fields (50 cm^2 total active area and 40 channels with *ca.* 0.4 mm wide land/channels) in a Greenlight test fixture.

MEA testing was performed using a Scribner 840 fuel cell test station supplied with ultrahigh purity H_2, O_2 and Ar gases (Praxair). H_2–air and H_2–O_2 measurements were made at 80 °C, 100% RH and 150 kPa_{abs}, with cathode and anode gas flow rates of 5000 and 500 sccm, respectively. Under this differential

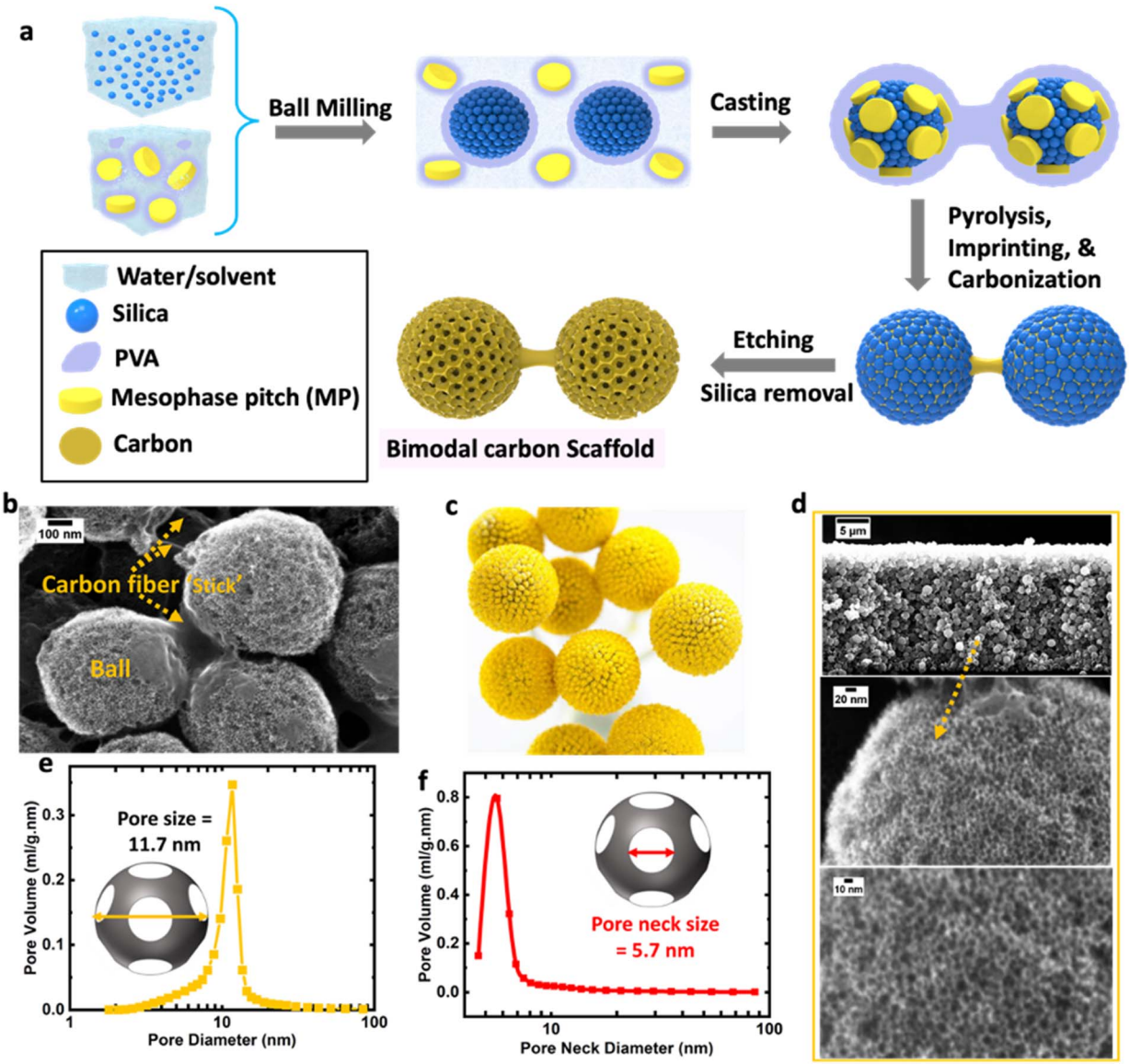

Fig. 1 Morphological and pore characteristics of self-supported 'ball-and-stick' BCS films. (a) Schematic of the process used to prepare the bimodal carbon scaffolds studied here. (b) FESEM top-down image of BCS film. (c) Photograph of analogous Craspedia flower structure. (d) Top to bottom: FESEM images of the cross-section of an 18 μm thick BCS film at low magnification, a closer look at one of the BCS spheres at higher magnification, and a still higher magnification image of the ordered 12 nm pores within the spheres. (e and f) Pore size distribution (PDS) of BCS films obtained from the N_2 gas sorption isotherm (BJH method), with (e) showing the adsorption branch, giving the average pore diameter, and (f) showing the desorption branch, giving the average pore neck size.

condition, the impact of the flow field could be minimized and the effect of catalyst layer structures can be differentiated. Specific details about the conditioning and measurement protocols used here were identical to those we reported in previous publications.[24,27] To establish a baseline comparison for the performance of BCS-based and NCS-based cathodes, a commercial catalyst-coated membrane (anode and cathode loadings of 0.1 and 0.4 mg_{Pt} cm^{-2}, respectively) was also evaluated under identical test conditions. To evaluate the Pt accessibility and proton transport properties of the Pt/BCS and Pt/NCS cathodes, cyclic voltammograms were collected at various relative humidities (*i.e.*, 30%, 50% and 80% RH). Accelerated durability tests (ADT) were performed using 10 000 square-wave potential cycles between 0.6 V and 0.95 V, with 3-second holds at each potential. These ADTs were performed under H_2–Ar at 80 °C, 100% RH and 150 kPa_{abs}, with cathode and anode gas flow rates of 1000 and 1000 sccm, respectively.

Results and discussion

Morphology and internal structure of bimodal carbon scaffolds

The bimodal ('ball and stick') carbon scaffolds (BCS) were prepared by mixing a colloidal suspension of silica (nominal 12 nm diameter) in a propanediol/water mixture with a mesophase pitch/*n*-butanol/polyvinylalcohol (PVA) ink (Fig. 1a). Similar to our prior work with self-supported carbon scaffolds with only a single pore size,[30–33] the resulting slurry was tape-casted on glass to achieve the desired thickness, dried, and heat-treated at 400 °C. This causes the 12 nm silica nanoparticles (NPs) to close-pack into spherical shapes and the mesophase pitch to then penetrate the gaps between the NPs within the spheres, leaving the voids between the spheres empty (Fig. 1a). These precursor films were then heated at 900 °C to achieve carbonization of the pitch, with the silica then removed completely in base after cooling. For the subsequent preparation of the BCS-based catalyst layers, Pt was deposited by atomic layer deposition (ALD), followed by Nafion (ionomer) impregnation.

We first probed the morphology of the BCS host material by scanning electron microscopy (FE-SEM), where Fig. 1b clearly illustrates the bimodal ('ball-and-stick') microstructure, with each ball (sphere) composed of a uniformly porous structure of 3-D interconnected and ordered 12 nm pores. Each sphere is tethered to its neighbors by carbon fibers ('sticks'), producing a mechanically robust scaffold, giving the BCS its self-supported character and holding the 100% carbon film together even in the absence of a binder. The carbon fibers (sticks) also provide the BCS film with the needed continuous 3D pathways for electron transport, giving the BCS its excellent through-plane conductivity.

The unique ball-and-stick nanostructure of the BCS material, shown in Fig. 1b, is the result of the conditions employed during its synthesis, including the use of polyvinyl alcohol to

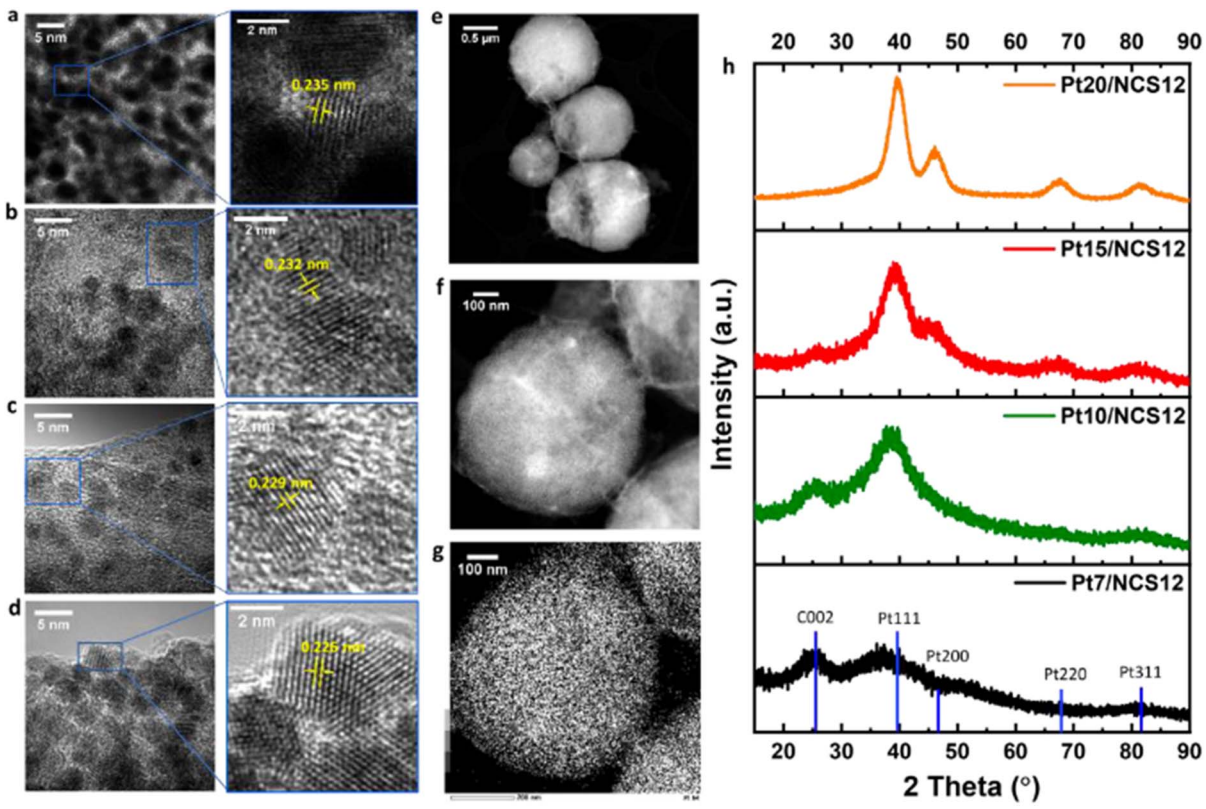

Fig. 2 Properties of ALD-Pt NPs on the BCS support. (a–d) High resolution transmission electron microscopy (HR-TEM) images of Pt7/BCS, Pt10/BCS, Pt15/BCS and Pt20/BCS, respectively. (e) and (f) Annular dark-field TEM images of the spheres within the Pt10/BCS at two different magnifications. (g) EDX map of Pt in Pt10/BCS. (h) XRD patterns of Ptx/BCS films (Pt XRD reference: PDF 04-0802).

accelerate and catalyze the agglomeration of the 12 nm colloidal silica particles into spheres that are *ca.* 1 μm in diameter. During imprinting at 400 °C, the mesophase pitch penetrates the close-packed silica-based spheres, leaving the voids between the spheres empty. The PVA concentration also plays an important role in controlling the formation and properties of the fibers ('sticks') that connect the spheres together, with the cartoon shown in Fig. S1 showing the relevant chemistry involved and how/why the ball-and-stick structure is obtained when preparing the BCS. It should also be noted that the desired microstructure has been achieved only after careful optimization of the ratio of the silica, PVA, and MP components during BCS preparation.

The larger secondary pores found between the spheres give the BCS its desired bimodal porosity, somewhat reminiscent of the *Craspedia* flower (Fig. 1c). The spheres are quite uniform in size (0.95 ± 0.17 μm diameter, Fig. S2), with the connecting fibers being non-porous and roughly 20 nm in diameter. Fig. 1d shows a cross-sectional view at several magnifications of an 18 μm thick BCS, revealing excellent thickness uniformity with the same features retained throughout the film in 3-dimensions, providing an organized and reproducible micro-environment throughout the scaffold. After silica removal, the BCS films contain only carbon, giving the expected XRD pattern after carbonization at 900 °C (Fig. S3).

Notably, the internal dimensions of each feature within the BCS can be easily tuned by minor variations in the preparation conditions. For example, by altering the PVA : silica ratio from 1 : 1 to 1 : 2, less void space can be imparted to the BCS (Fig. S4). The ball-and-stick morphology of the BCS arises from a combination of the small silica template size used here (12 nm) and the presence of PVA, which promotes the agglomeration of the 12 nm colloidal silica particles into spherical shapes and also leads to carbon fiber (stick) formation.

The BCS morphology is very different from the monodisperse porosity designed into our previously reported colloid imprinted carbon (CIC) powders with 10 (or larger) nm pore sizes as well as our nanoporous carbon scaffolds (NCS),[30,33] which were designed to contain pores of only one size (10–100+ nm in diameter). This was achieved by employing the desired size of the silica particle template. Fig. S5 shows the very different morphology of the NCS materials *vs.* the BCS material

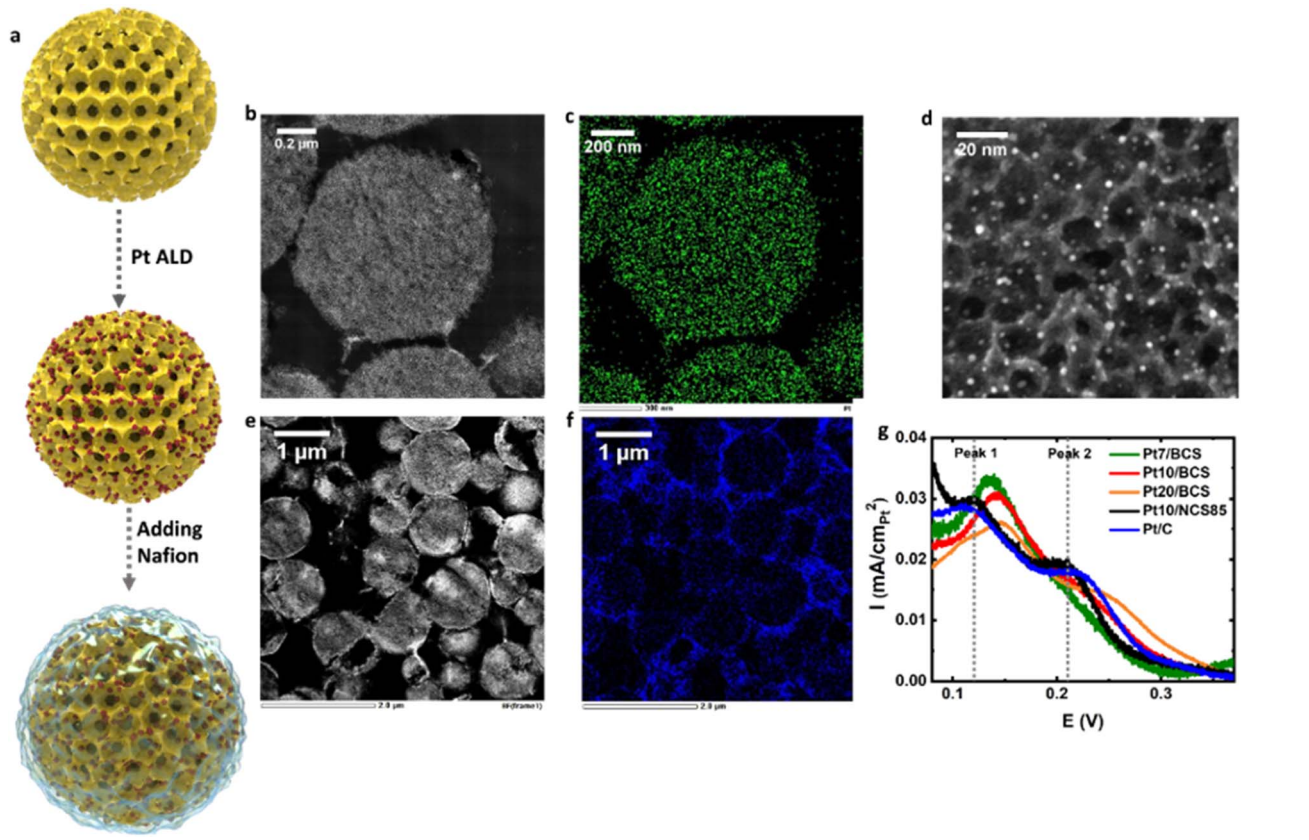

Fig. 3 Design and characterization of ALD Ptx/BCS catalyst layer with Pt inside the 12 nm pores within the spheres and Nafion present only on the outer sphere surfaces. (a) Schematic illustration of the steps required to first load Pt using *x* ALD cycles and then infiltrate Nafion into the BCS. (b) High annular dark-field scanning transmission electron microscope (HAADF-STEM) image, (c) Pt EDX map (green), and (d) HAADF-STEM image of a cross-sectional sample, all of a Pt10/BCS film, showing the rich presence and excellent distribution of Pt NPs within the 12 nm pores inside the spheres. (e) HAADF-STEM micrograph of a 100 nm microtomed slice of the Pt10/BCS catalyst layer in an MEA, showing its microstructure, and f, its associated fluorine EDX map (blue), indicating that Nafion is distributed only on the outer sphere surfaces in the Pt10/BCS sample. (g) Cyclic voltammetry (CVs, 20 mV s^{-1}, 100% humidified Ar at 80 °C) of the Ptx/BCS (where $x = 7$, 10 and 20) compared to a Pt10/NCS85 membrane and a state-of-the-art Pt/C powder-based catalyst, all in an MEA in H_2/Ar at 80 °C and at 100% RH.

(Fig. 1), with the two NCS examples demonstrating a monodisperse 50 nm (Fig. S5a) and 85 nm (Fig. S5b) pore size. Here, the monodisperse NCS85 scaffold is used as a comparison catalyst support material for membrane-electrode-assembly (MEA) and accelerated durability testing (ADT) of the bimodal carbon scaffolds after Pt loading.

While the BCS morphology was designed to be highly open in order to facilitate mass transport of fluids, the BET-determined surface area of the BCS film is still quite high ($\sim$610 m^2 g^{-1}), with the mesoporous and microporous surface areas being $\sim$545 and $\sim$65 m^2 g^{-1}, respectively (Table S1). Unlike previously reported monolithic carbon spheres,[37] the main sources of porosity and surface area of the BCS originate from the spheres themselves, as the fibers are likely non-porous. Also, the scalability of the BCS films in terms of their geometric surface area (from a few cm^2 to 100 cm^2) is unprecedented. Nitrogen sorption analysis (Fig. S6) reveals a Type IV isotherm, with the observed hysteresis being due to capillary condensation within the 12 nm mesopores, combined with the presence of the smaller pore necks inside the spheres.[38] Using the Barrett–Joyner–Halenda (BJH) method, the pore size distribution of BCS was obtained from the adsorption branch (Fig. 1e), with the narrow peak at 11.5–12 nm confirming an excellent microstructural uniformity within the spheres. Using the desorption data (Fig. 1f), the BJH method gives an average pore neck diameter of 5.7 nm, with 12 necks present per mesopore within the spheres. Roughly 98% of the BET surface area originates from the 12 nm pores in the spheres, while the outer surface of the spheres plus the sticks contribute to the remaining surface area (Table S2).

ALD loading of Pt into 12 nm primary pores in bimodal carbon scaffolds (BCS)

The BCS material was loaded with Pt nanoparticles (NPs) using a range of ALD cycles (7, 10, 15, and 20), with the ultimate goal being to monitor their micro-environment by imaging and tracking their electrochemical properties, then determining their electrochemical activity towards the oxygen reduction reaction (ORR) in a PEMFC membrane electrode assembly (MEA). Here, we refer to the Pt-loaded BCS material as Pt*x*/BCS*y*, where *x* depicts the number of Pt ALD cycles used and *y* is the BCS pore size (12 nm).

High-resolution TEM analysis (Fig. S7) reveals that the Pt NP size within the spheres is 1.5 $\pm$ 0.3 nm, 2.4 $\pm$ 0.4 nm, 2.6 $\pm$ 0.4 nm, and 3.6 $\pm$ 0.6 nm after applying 7×, 10×, 15×, and 20× ALD-Pt cycles, respectively, with a narrow particle size distribution consistently observed. We also noted that the Pt NPs began to nucleate on the outer surface of the spheres only after 20+ ALD cycles were applied. This shows that both the size and location of the Pt NPs can be controlled within the BCS by the number of ALD steps employed, arguing for some preference for Pt deposition inside the 12 nm pores, as these are the ones that fill first. The Pt NPs in the Pt*x*/BCS sheets are also highly crystalline in nature, with clear lattice spacings seen (Fig. 2a–d).

Fig. 2e–g show a series of lower magnification TEM (bright field) images of the Pt/BCS material, clearly revealing the sphere morphology and that they are well-connected to the carbon fibers (Fig. 2e and f), even after multiple Pt ALD cycles that were interspersed with time spent at 190 °C in several different atmospheres (Ar, air and vacuum). This verifies the robustness of the BCS materials, where their unique morphological and microstructural characteristics are completely retained after the ALD process is complete. Importantly, a uniform distribution of Pt NPs is seen throughout the interior surfaces of the 12 nm pores in each individual NCS12 sphere, as confirmed by the Pt EDX scan of Pt10/BCS, as an example, in Fig. 2g.

As the NP size increases, the lattice fringes become even more obvious (Fig. 2a–d), with the HRTEM images giving a lattice spacing of *ca.* 0.226 nm, typical of Pt111 facets.[39] Interestingly, the corresponding Pt111 lattice fringes tend to expand when a low number of Pt ALD cycles is used, indicative of the presence of some lattice strain in the smaller Pt NPs. This is also confirmed by XRD analysis (Fig. 2h), where a shift relative to the Pt reference (PDF 04-0802) further supports the presence of strain. It is interesting to note that the presence of strain has been stated to boost the activity of Pt NPs toward the ORR in other work.[40,41] It is worth mentioning that the absence of the carbon (002) peak in the XRD pattern of Pt20/BCS is attributed to its high platinum mass loading ($\sim$1 mg_{Pt} cm^{-2} and $\sim$60 wt% Pt), resulting in the dominant intensity of the Pt diffraction peaks.

Unique micro-environments of Pt and Nafion in BCS catalyst layers

Without the addition of specific ORR catalysts, such as Pt or heteroatom dopants, it is known that carbon materials are inactive towards the ORR in the acidic environment within PEMFCs. Therefore, to evaluate the BCS films as a catalyst layer in a membrane-electrode-assembly (MEA), Pt and Nafion were loaded sequentially into the scaffolds, with Fig. 3a showing a simple schematic illustration of the fabrication steps used. The Pt nanoparticles (NPs) were loaded first in *x* cycles of Pt atomic layer deposition (ALD). The ALD-Pt precursor (methylcyclo-pentadienyl trimethyl-platinum (MeCpPt-Me3)) is $\sim$1 nm in its longest dimension, which is significantly smaller than the $\sim$12 nm pores and $\sim$6 nm pore necks inside the BCS spheres. It was therefore predicted that there would be no difficulty in accessing all of the internal surfaces of the BCS during atomic deposition of Pt, considering its highly open porosity and excellent line-of-sight microstructure.

Scanning transmission electron microscopy (HAADF STEM, Fig. 3b) and EDX mapping of Pt within the individual spheres (Fig. 3c) and across the full thickness of both a 7 and a 10 ALD cycle film (Fig. S8) confirm that this is indeed the case, with Pt NPs uniformly distributed throughout the BCS. At a higher magnification, the HAADF STEM images in Fig. 3d and related STEM images of a Pt/BCS sheet loaded with Pt in 10 ALD cycles (Fig. S9), as well as TEM images of the microtomed the Pt10/BCS (Fig. S10), confirm that the 12 nm internal pores inside the spheres are uniformly decorated with highly dispersed Pt NPs. We also determined the oxidation state of Pt in the Pt10/BCS sample by analyzing the Pt 4f X-ray photoelectron

spectroscopy (XPS) data, revealing the presence primarily of metallic Pt. Evidence for the presence of Pt oxide (with Pt in the +II and +IV states) is also seen, attributed to air exposure of the Pt NPs after the ALD process and before XPS analysis (Fig. S11).

The ALD Pt-loaded BCS was then placed on a gas diffusion layer/microporous layer (GDL/MPL) and loaded with Nafion by drop-casting a Nafion solution onto the Pt/BCS films. Following this step, STEM imaging and EDX mapping for fluorine (Fig. 3e and f, respectively) on the cross-sections showed that the ionomer is very well distributed in the large 250 ± 40 nm secondary pores between the spheres, coating them well and also surrounding the connecting carbon fibers, providing a 3-D inter-connected pathway for proton transport across the scaffolds. However, no fluorine was found inside the 12 nm pores within the spheres (Fig. 3f), the region where the vast majority of the Pt NPs reside. This is consistent with previous literature[24] that has shown that Nafion cannot penetrate pores less than 20 nm in size. Thus, Nafion would be incapable of accessing the BCS spheres, especially considering their much smaller neck diameters (~6 nm, Table S1). The result is a bimodal porous carbon scaffold containing both Pt and Nafion, but with these phases fully separated from each other. This has raised the question as to how muted the electrochemistry of the Pt NPs would be in the MEA and, if the Pt NPs are indeed active, what their response would be without any interference from nearby Nafion.

Ultra-high ECSA and unique hydrogen adsorption/desorption characteristics of ALD-Pt NPs in bimodal carbon scaffolds

To answer this, the Pt/Nafion-loaded BCS materials were loaded as a cathode catalyst layer into an MEA along with a conventional high activity Pt/carbon anode layer, and the cathode electrochemistry was evaluated using cyclic voltammetry in humidified argon. One objective was to determine the electrochemically active surface area (ECSA) of the Pt NPs at the various ALD Pt loadings in the absence of Nafion by tracking the hydrogen underpotential adsorption/desorption (HUPD) peak charges in cyclic voltammetry experiments. Fig. S12 shows that all of the Pt/BCS cathode layers do show the HUPD peaks, with Pt10/BCS giving an exceptionally high ECSA of ~130 $m^2\ g^{-1}$ in the MEA (Table S3). This ECSA is comparable to what was observed when cyclic voltammetry of a small piece, cut from the larger ALD-loaded BCS, was run in 0.5 M H_2SO_4 (Fig. S13), which gave a very similar ECSA of ~140 $m^2\ g^{-1}$. Pt7/BCS is a close second, also with a very high ECSA value of ~100 $m^2\ g^{-1}$, as compared to typical values of ~75 $m^2\ g_{Pt}{}^{-1}$ in MEAs constructed from conventional Pt/carbon powders.[42] These high ECSA values may be attributed to the high density of oxygen functional groups combined with the large surface area of the BCS, both of which facilitate uniform Pt deposition *via* ALD and promote the formation of small Pt NPs.

These electrochemically-determined ECSA values were compared as a percentage of what would be expected based on the total area of the Pt NPs, as seen from TEM particle size analysis (Fig. S7), giving a value of ~100% for both Pt10/BCS and Pt20/BCS (Table S3). It is therefore noteworthy that, for these two catalyst layers, essentially all of the Pt NPs are active under ORR kinetically-controlled conditions, even those that are located deep inside the 12 nm pores that are internal to the ~1 μm spheres and located quite far from the ionomer that envelops the spheres (Fig. 3f). To put this into perspective, the mesopore length in the carbon powders studied by Yarlagadda *et al.*[24] was in the range of 50–100 nm, while the length of the pores in the present work inside BCS spheres is 200–400 nm.

In the absence of proximal Nafion in our case, protons must therefore be transported over relatively long distances to/from the Pt NPs that are inside the BCS spheres by some other means, likely through water, as discussed in more detail below. This, in turn, means that Nafion poisoning of the Pt NP surfaces should not be seen. In comparison, Table S3 shows that the comparison scaffold material, Pt10/NCS85, in which Nafion can easily access the 85 nm pores and *ca.* 16 nm pore necks, exhibits an ECSA that is only 70% of the theoretical ECSA calculated from the TEM particle size analysis. Overall, these results predict that the Pt10/BCS catalyst layer should be the best of all, considering its very high ECSA value in the MEA.

It is also notable that distinctive differences in the HUPD peak potentials are observed (Fig. 3g and Table S4) for the ALD-Pt*x*/Nafion/BCS catalysts compared to what is seen at conventional Pt/Nafion/carbon powder materials, where the Pt NPs, residing on the outer surface of the carbon particles, are in direct contact with Nafion. The HUPD potentials are also quite different from what is observed at ALD-Pt hosted within the NCS-85 comparison material, where the 85 nm pores easily allow Nafion penetration. For these latter two cases, where Pt and Nafion are in the same micro-environment, oxidation peaks 1 and 2 are centered at 0.11–0.12 V and 0.21–0.22 V, respectively, typical also of what is seen at Pt NPs in most commercial MEAs.[43–45] Peak 1 has been ascribed to HUPD at Pt(110) surfaces, while peak 2 has been attributed to more strongly adsorbed H at Pt(100) and/or Pt(111) surfaces.[44–46]

In comparison, all of the BCS catalysts show a 20–30 mV positive shift in peak 1, now centered at around ~0.14 V (Table S4). Also, for 20 or more cycles of ALD, peak 2 emerges, but it too is shifted positively (by 30–40 mV), from ~0.21 V to ~0.25 V. It has been reported that anions that specifically adsorb on Pt, *e.g.*, sulfate, chloride, and bisulfate,[47] cause a negative shift of the HUPD peaks on Pt, as they compete with H atoms for Pt surface sites.[48–50] As the Nafion sulfonate group is also known to adsorb (and poison) Pt surfaces,[13–16] the observed more positive potentials of both of the HUPD peaks in the Pt/BCS catalysts therefore further supports the argument that the Pt NPs are in a Nafion-free micro-environment when supported by the BCS materials.

High oxygen reduction mass and specific activities during MEA testing

While the full Pt NP ECSA was active in HUPD experiments in the MEA, a key question was whether the ALD Pt/BCS materials would be active towards the oxygen reduction (ORR) reaction, even at relatively low current densities, considering that oxygen must reach the Pt NPs and as no Nafion is nearby to provide protons. Therefore, the ORR activity of the Pt*x*/BCS-based

catalyst layers, the Pt10/NCS85 comparison material, and the commercial Pt/C catalyst, were evaluated in side-by-side MEA testing in a H_2/O_2 environment at 80 °C, also comparing with the leading results reported to date in the literature (Table S5). Remarkably high ORR activities were seen, with the best performance shown by Pt10/BCS, the cathode catalyst layer in which the full Pt ECSA was obtained and where essentially all of the Pt NPs are in a Nafion-free environment. This catalyst gave an average mass-normalized ORR activity of 0.58 A mg_{Pt}^{-1} at low current densities, calculated by dividing the current density by the Pt mass loading of each sample (at 0.9 V) (Fig. 4a and b), which is a 1.5 to 2-fold enhancement compared to the best that can be delivered by previously reported Pt/C catalysts.[7,42] Moreover, this is also a 3-fold enhancement relative to the performance of both the commercial Pt/C (tested here under the same low current density conditions of this study) and the ALD-Pt10/NCS85 material, with its large, Nafion-accessible, 85 nm pores (Fig. 4a, b and Table S5). The Pt10/BCS catalyst layer also gives ~1.3 times the mass activity of the Department of Energy (DOE) 2025 targets (0.44 A mg_{Pt}^{-1}) at 0.9 V. While it is acknowledged that Pt alloy catalysts can exhibit still higher mass activities, the value reported here represents a significant leap over that of most previously well-studied pure Pt catalysts (Table S5).[7,42,51]

Using another dimension of comparison, Fig. S14 shows the ORR activity at 0.9 V, normalized to the Pt ECSA, giving the specific activity (SA, the intrinsic catalytic activity of a particular Pt surface) (Table S5). Despite their smaller NP sizes, the Pt7/BCS and Pt10/BCS catalyst layers, in which the Pt NPs are entirely inside the spheres, give a SA as high as 0.45 mA cm_{Pt}^{-2}, which is significantly higher than reported for most other state-of-the-art Pt/C powder catalyst layers (0.31 mA cm_{Pt}^{-2}, ref. 42), but similar to Pt(ALD)/Ketjen Black.[28] Furthermore, for the same number of ALD cycles and similar Pt NP sizes, the Pt NPs in Pt10/BCS still exhibit twice the SA at 0.9 V than in Pt10/NCS85, even though the average Pt NP size in Pt10/NCS85 (Fig. S15) is essentially the same (2.2 nm) as in Pt10/BCS (Fig. S7b).

This improvement in the oxygen reduction kinetics, based on either the real Pt area (SA) or the mass of Pt used (MA), is unrelated to either NP size or the ECSA values but instead is the consequence of the nano-engineered ball-and-stick microstructure of the BCS catalyst layer, which serves to screen the Pt NPs from direct contact with Nafion. This then explains the high MA and SA values observed, especially for Pt10/BCS, with the protons required for the ORR supplied locally by water. This is also supported by the observed lower MA and SA values for the ORR at Pt20/BCS, where Pt has now begun to deposit on the outer sphere surfaces where Nafion is co-located and can adsorb on the Pt NP surfaces.

The role of water in providing protons to the Pt NPs within the 12 nm BCS pores during the ORR was verified by altering the relative humidity (RH) during the running of CVs using the MEA.[24] Fig. 4c shows a significant decrease of ~50% in the HUPD charge for ALD-Pt10/BCS at lower RH, supporting the supposition that water is the source of proton conductivity within the 12 nm pores inside the spheres, where the active Pt

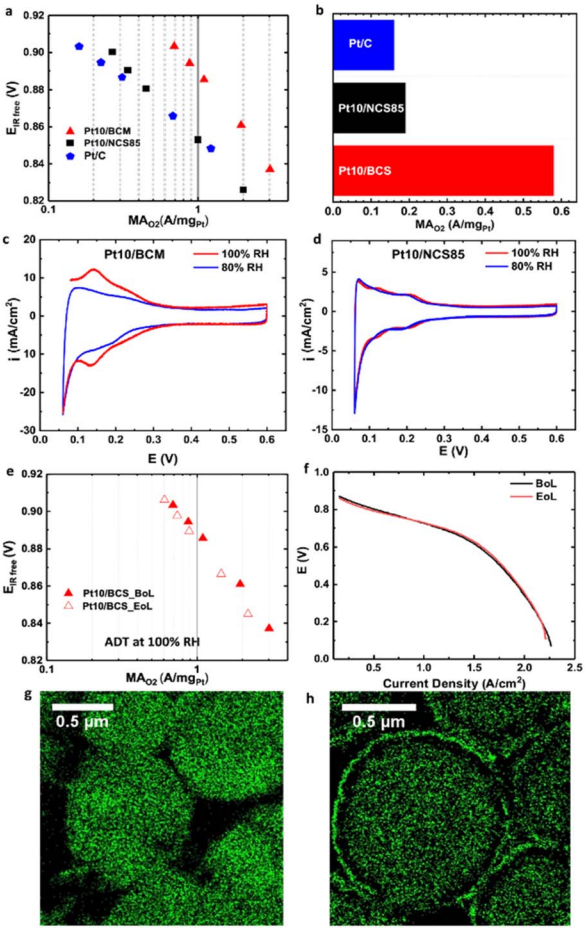

Fig. 4 Electrochemical performance and durability of self-supported Pt10/BCS catalyst layers in PEMFC MEAs. (a) *iR*-Corrected H_2/O_2 mass activities at 100% RH, 150 kPa_{abs}, and 80 °C. (b) Average mass activity at 0.9 V for 3 repeat samples. (c and d) CVs (20 mV s^{-1}, humidified H_2/Ar at 80 °C) of (c) Pt10/BCS and (d) Pt10/NCS85 catalyst layers, measured at RH values of 80% and 100%. (e) H_2/O_2 mass activity of P10/BCS at BoL and EoL, collected after 10 000 square-wave cycles between 0.6 V and 0.95 V, with 3 second holds at each potential. (f) *iR*-Corrected H_2/air performance of MEAs of Pt10/BCS at BoL and EoL at 100% RH, 150 kPa_{abs}, and 80 °C. (g and h) Pt EDX mapping (green = Pt) of Pt10/BCS catalyst layer in the MEA at (g) BoL and (h) EoL. In (c) Pt10/BCM is Pt10/BCS.

NPs reside. In contrast, minimal changes in the HUPD charges are observed for Pt10/NCS85 (Fig. 4d) with changing RH, where the Pt NPs are in direct contact with the ionomer that can easily access the 85 nm pores.[30] Several prior studies have argued in support of transport of protons through water during the ORR in MEAs, but only over shorter distances than observed here.[4,52–55]

In earlier investigations of Pt NP-decorated mesoporous carbons,[1–4,23,56] all of which contain pores that are too narrow for Nafion to access, the ORR was proposed to occur by proton transport through liquid water generated by the ORR over distances of 30–50 nm. Using these types of carbons, Yarlagadda and coworkers[24] generated a high MA of 0.36 A/mg_{Pt}, attributing this to avoidance of ionomer poisoning, with proton

transport suggested to occur *via* water over lengths of 40–50 nm. In other work, Gasteiger *et al.*[42] assumed that water adsorbed on the inner surface of ~50 nm long mesopores within Ketjen Black powder can conduct protons to the Pt NPs during the ORR. The ultra-high MA values seen for Pt NPs within the BCS spheres in the present work, combined with the significant effect of RH on the ORR kinetics, therefore demonstrate that protons can be carried to the Pt NPs by surface water over still longer distances than in these previous reports.

Why are Pt NPs in Nafion-free micro-environments so electrocatalytically active?

Additional strong support for the facile transport of protons through the Nafion-free pores within the BCS spheres was obtained from an entirely different set of experiments, namely the evaluation of the performance of the Pt/BCS catalyst layer in an MEA without any Nafion added (*i.e.*, Nafion-free conditions), as shown in Fig. S16 and S17. Unexpectedly, it is seen that close to the full Pt ECSA is obtained at low current densities (ECSA without any Nafion added is 103 $m_{Pt}^2\ g_{Pt}^{-1}$ as compared to an ECSA with Nafion infiltrated of $100 \pm 20\ m_{Pt}^2\ g_{Pt}^{-1}$), even in the complete absence of any Nafion throughout the 18 μm BCS thickness, as shown in Fig. S16. Furthermore, the H_2/air MEA performance with no Nafion added is also surprisingly reasonable at low current densities (Fig. S17), making our Pt/BCS CL the first Pt/carbon-supported material that performs similarly to the ionomer-free and carbon-free 3M NSTF (nanostructured thin film)[57] in an MEA. Overall, our results demonstrate conclusively that the Pt NPs within the 12 nm pores inside the BCS spheres are highly ORR-active at low current densities, even in the complete absence of any Nafion within the ALD Pt/BCS catalyst layers.

One possible model to explain the very high ORR mass and specific activity (at 0.9 V) of the ALD Pt NPs in the BCS over these long distances in the absence of accessible Nafion involves proton transport *via* a contiguous nanostructured ALD-produced ultra-thin film (NSTF) of Pt that electrically connects neighboring Pt NPs, similar to what was first developed by 3M.[57] However, given the very different response of the Pt10/BCS and Pt10/NCS85 catalyst layers to RH (Fig. 4c *vs.* d, respectively), both containing ALD-Pt, the hypothesized thin film structure of Pt between Pt NPs inside the BCS spheres seems unlikely.

A more rigorous explanation for the long distance of proton transport achieved within the Nafion-free BCS spheres is related to the unusually high density of surface oxygen-functionalities on the inner BCS pore surfaces, consistent with the pronounced internal hydrophilicity of the spheres and of the BCS overall.[30,31,58] The concentration of surface oxygen groups is significantly higher (by 6 times) in the BCS than in Ketjen Black-300J, for example, as measured using temperature-programmed desorption (TPD) analysis under identical conditions (Fig. S18 and Table S6).[59] X-ray photoelectron spectroscopy (XPS) of the BCS was carried out to confirm this, with the O 1s and C 1s XPS patterns in Fig. S19 and the data in Table S7 clearly showing the presence of significant C–O, C═O and C–OH surface functionalities. Furthermore, the cyclic voltammetry response of the bare BCS carried out in 0.5 M H_2SO_4 (Fig. S20) displayed large pseudocapacitance peaks, centered at 0.6 V *vs.* RHE, which are associated with multiple surface oxygen redox processes, consistent with an oxygen-rich hydrophilic character. The resulting high degree of surface wettability was also confirmed from the measured deionized water contact angle, shown in Fig. S20b to be *ca.* 56°. These highly oxygen-rich surface sites should therefore be readily deprotonated in the humidified MEA environment, facilitating proton transport along the BCS surface to the Pt catalyst during oxygen reduction.

The observed ease of proton transport along the wet surfaces of the 12 nm pores, combined with the absence of any Nafion poisoning effects, would then explain the high ORR activity observed in the kinetic region (Fig. 4a) over Nafion-free lengths of several hundred nm, extending from the surface to the core of the BCS spheres. As stated above, this hypothesis has been verified by the marked sensitivity of the ECSA of the Pt10/BCS to RH (Fig. 4c) and the unexpectedly high ECSA and reasonable ORR activity at low current densities, even in a Pt/BCS catalyst layer containing no Nafion at all. Recognizing that surface water is most likely the sole transport medium for protons to the Pt NPs inside the spheres, the Pt/BCS catalyst layer exhibits the superior ORR kinetics expected from a micro-environment that is completely free of Nafion poisoning effects. Recognizing that surface water is most likely the sole transport medium for protons to the Pt NPs inside the spheres, the Pt/BCS catalyst layer exhibits the superior ORR kinetics expected from a micro-environment that is completely free of Nafion poisoning effects.

Table S8 summarizes the performance in terms of power densities in air/H_2 for all Pt*x*/BCS catalyst layers examined here, in comparison with our benchmark catalysts (the commercial Pt/C and the monodisperse Pt10/NCS85). This shows that the commercial Pt/C CL does outperform the Pt*x*/BCS CLs at high current densities, as also seen in Fig. S21, where a limiting current is reached for Pt/BCS but not for Pt/C. This is likely due to the substantially thicker catalyst layer (18 μm) used for Pt*x*/BCS *vs.* the <10 μm thickness of the commercial Pt/C. Challenges are also expected in moving protons and oxygen rapidly through the Nafion-free 12 nm pores and their 5–6 nm pore necks over lengths of several hundred nm. A closer examination of Fig. S21 shows that the best-performing Pt7/BCS and Pt10/BCS materials at high current densities have the highest Pt ECSA values (Table S3) and thus the local oxygen transport resistance is expected to be the lowest. As explained by Kongkanand and Mathias,[23] electrodes with high roughness factors ($cm_{Pt}^2\ cm_{MEA}^{-2}$) generally show lower O_2 transport resistance due to the presence of Knudsen diffusion in small pores (<100 nm diameter) and/or due to diffusion through liquid water or ionomeric films. As more O_2 must be delivered to a larger Pt surface area, this results in a lower apparent electrode O_2 transport resistance, consistent with what is seen in Fig. S21. The Pt NPs in the leading Pt7/BCS and Pt10/BCS materials at high current densities (Fig. S21) are also the smallest, being only *ca.* 2 nm in size (Fig. S7), which would be expected to only minimally hinder mass transport by a pore blocking effect. This is in contrast to the situation in Pt20/BCS,

where the Pt NP size is *ca.* 3.5 nm, which is more than half the diameter of the pore necks located between adjacent pores.

For the completely Nafion-free Pt/BCS catalyst layers (Fig. S17), as expected, the performance in air at high current densities is very poor compared to the same Pt/BCS catalyst layer (with the same Pt loading) but after Nafion was infiltrated. While the proton and oxygen transport rates within the Nafion-free 12 nm pores may still be very good, without any Nafion present in the large secondary pores between the BCS spheres, proton transport across the full BCS layers will be severely hindered, especially at high current densities. These secondary pores must serve the same role in housing Nafion as those found in archetypical powder-based Pt/carbon catalyst layers between the carbon particles (secondary pores), which can range from 20 to <200 nm in size.[60]

Retention of oxygen reduction kinetics after accelerated degradation testing

To investigate the long-term performance stability of the Pt NPs in the absence of any Nafion within the BCS catalyst layers, 100% RH accelerated durability testing (ADT) was applied to the best performing cathode, namely Pt10/BCS, following the DOE protocol.[61] Fig. 4e shows the ORR kinetics at both the beginning of life (BoL) and end of life (EoL), revealing that the Pt mass-normalized ORR activity at low current densities has hardly changed, while the specific activity (Table S8) increased dramatically after ADT at 100% RH. Fig. 4f shows the full performance curve, revealing only a minor extent of degradation at high current densities, translating to a less than 20 mV loss in the H_2–air performance. Fig. S22 and S23 show TEM images of the structure of the BCS before and after ADT, respectively, revealing that the BCS spheres are still fully intact.

At the same time, a loss of Pt ECSA of roughly 55% is seen from the Hupd regions in the CVs, collected in the MEA (Fig. S24) under a humidified Ar environment at the cathode after ADT. This is consistent with what is seen from TEM analysis (Fig. S25), which reveals ripening of the Pt NPs after ADT at 100% RH, with an increasing size seen both inside and on the outer surface of the BCS spheres. Further evidence for Pt aggregation was obtained by comparing the TEM images in Fig. S6 with those in Fig. S25(a–c), showing that the average Pt particle size increased from ~2.5 nm at BoL to 4.5–5 nm at EOL (Table S9). HR-TEM further revealed that a region that extends roughly 50 nm below the sphere surfaces is Pt-depleted after ADT (Fig. S25), with the EDX line scans across the sphere supporting this in Fig. S26, while also showing that Nafion has remained coated on the outer sphere surfaces. These results demonstrate that the NPs in the sub-surface region are particularly prone to particle migration and ripening, in agreement with the Pt EDX mapping in Fig. 4g and h, perhaps due to their proximity to Nafion. These fine details would be very difficult to observe in traditional catalyst systems, where Pt NPs tethered to the surface of randomly located carbon particles are intermingled with surrounding ionomer. However, when examining these self-supported and highly organized BCS films, we can clearly discern the fate of the NPs, while also being certain that Nafion and Pt remain well-shielded from each other.

One explanation for the retention and even improvement in ORR kinetic activity at the low current densities at which mass transport effects can be ruled out (Fig. 4 and Table S8), even while the average Pt NP size increased, is compensation by a higher surface density of more catalytically active Pt facets ('the particle size effect'). This phenomenon, reached when Pt NP are ~5 nm in size, has been observed previously by various peer groups[55,56] and also by us[57] and could be part of the explanation. Note also that it is not possible that the initial ORR mass activity is based on an over-estimation of the ECSA of the initially active Pt NPs, as this would then equate to an under-estimation of the original mass activity of the Pt nanoparticles. If this had been the case, we should have observed a still higher mass activity in our Pt10/NCS85 control sample (Fig. 4b), where all of the Pt NPs are in very close proximity to Nafion, even while the ALD-Pt NP sizes are very similar to that in the Pt10/BCS catalysts. However, the experimental results indicate that the opposite is true.

It is also possible that the Pt NPs are being stabilized inside the BCS spheres during ADT by the rich density of oxygen-rich sites on the BCS surface, based on previous reports that C═O groups and negatively charged surface oxygen functional groups can influence both Pt NP retention and NP distribution, acting as anchoring centers to hinder agglomeration and surface diffusion of Pt nanoparticles across the carbon surface.[62] In the present work, verification of the rich surface density of oxygen groups on the BCS surface and its related exceptionally hydrophilic nature has been confirmed through cyclic voltammetry, DI water contact angle measurements, and TPD analysis (Fig. S18–S20, Tables S6 and S7), thus making the surface properties of the BCS highly relevant to the retention of the ORR kinetics under ADT conditions and the non-altered size and distribution of the vast majority of the Pt NPs within the BCS spheres.

The fact that there is no Nafion in the vicinity of most of the Pt NPs may also be relevant, as many papers have shown that Nafion can stabilize Pt NPs from dissolution.[34,61] Indeed, we have shown extensive TEM and other imaging evidence demonstrating that the vast majority of the Pt NPs are located far away from Nafion in the ALD Pt/BCS catalyst layers. Further, the significant differences in the effect of lowering the RH on the performance of Pt/BCS as compared to the comparison material Pt/NCS85, in which Pt and Nafion are in very close proximity to each other, also supports this argument. Given the results shown in Fig. S27, it is clear that a lowered RH minimizes Pt dissolution in the BCS structure, as shown by the much smaller ECSA losses (Fig. S27), thus confirming that the Pt NPs are in a water-based environment, not Nafion. However, in the monodisperse pore size control sample (Pt10/NCS85), where a lowered RH has minimal impact on proton accessibility (Fig. 4d), the influence of RH on Pt dissolution is much more pronounced. This is shown by significantly less preservation of the ECSA when Nafion is in direct contact with the Pt NPs.

A pore confinement effect may also be relevant in stabilizing the Pt NPs after ADT of these ALD Pt/BCS catalyst layers. This is because the 4–5 nm Pt NPs (after ADT, Fig. S25) are very similar in size to the pore neck in the BCS material, which is in the range of 5–6 nm (Fig. 1f). To summarize, any or all of the three

factors discussed above may explain the excellent retention of the mass activity and performance of the Pt NPs in the ALD Pt/BCS catalyst layers, also confirmed by the absence of any Pt in the Nafion separator after ADT testing.

To attempt to further confirm the bimodal proton conduction pathways within the BCS, with protons moving through the ionomer phase between spheres but moving through only water inside the Pt-containing spheres, we modulated the relative humidity during ADT. As discussed above, lowering the RH can deactivate water-based proton transport pathways but should still retain the Nafion pathways.[7,8] Therefore, for the BCS material, only the small fraction of Pt NPs within reach of the Nafion that is located only on the outer surface of the BCS spheres will be accessible to protons during ADT, and thus, the Pt NPs deeper inside the spheres should be unaffected by the ADT procedure. By comparing Fig. S27a and b, it is confirmed that the Pt ECSA is significantly better preserved after ADT of Pt10/BCS at the lower 80% RH (green bar), losing only ~20% of the active area *vs.* a loss of ~55% at 100% RH (red bar). Importantly, these losses are both significantly less pronounced than seen for the Pt10/NCS85 comparison material after ADT (loss of ~50% at ~80% RH (yellow bar) and a loss of ~65% at 100% RHE (black bar) for the commercial Pt/C benchmark (blue bar)), catalyst layers in which Nafion is in close proximity to the vast majority of Pt NPs.

Fig. S28 shows another highly beneficial outcome of the exposure of the best-performing ALD-Pt10/BCS catalyst to lower RH during degradation testing, displaying not only a retention of the ORR mass activity (MA) but an actual improvement in the MA for Pt10/BCS of up to 130% at low current densities (0.9 V, Fig. S28, right) at 80 and 100% RHE and also at higher current densities (0.75 V, Fig. S28, middle) as compared to the MA at BoL. This activation is observed in both O_2 at 0.9 V (low current densities (LCD), Fig. S28, right) and in air at 0.75 V (high current densities (HCD)) at 80% RH. As indicated, the degradation reversal is the most pronounced under low current density conditions, likely because the ripening process at 80% RH results in Pt NP sizes that are smaller than those under 100% RH.

It is hypothesized that the exemplary resistance to degradation (Fig. 4e and f) of the ALD Pt NPs in the ball-and-stick microstructure, as well as the observed degradation reversal shown in the MA data in Fig. S28, are related to a combination of the high density of oxygen functionalities on the BCS surface that may help retain the Pt NPs and/or capture any Pt^{2+} that forms, the absence of proximal Nafion, as well as possible nanopore confinement effects. Considering that enhanced MEA durability is becoming as important, if not more important, than improving electrocatalytic activity, this phenomenon of degradation reversal is a very significant result. Together with the demonstrated higher activity of the Pt NPs in the Nafion-free environment, these durability results further emphasize the benefits of the ball-and-stick BCS structure in modulating proton accessibility as a practical tool for catalyst design.

Conclusions

This study introduces a nano-engineered bimodal carbon scaffold (BCS) that redefines proton transport in PEMFC cathodes by spatially separating the ionomer distribution from direct contact with the catalytic Pt nanoparticles (NPs) to prevent Nafion poisoning of the catalyst surfaces. The key innovation lies in the unique architecture of the BCS, with its bimodal porosity, and the leveraging of atomic layer deposition (ALD) to precisely localize the Pt NPs within the 3D-interconnected mesopores (12 nm pores) inside the spheres in the BCS. In contrast, Nafion infiltrates only the macropores between the spheres, thus minimizing sulfonate group poisoning of the Pt NPs and maintaining a low gas–ionomer resistance.

Another critical property of the BCS is its highly defective and oxygen-rich surface within the mesopores, unlike all commercial hydrophobic carbon black, such as Ketjen black. Proton transport to the Pt nanoparticles (NPs) that are confined within the 12 nm pores inside the 500–1000 nm spheres but are separated from Nafion is then potentially facilitated by the water-wetted internal surface of the BC at 100% RH. This eliminates the need for direct Nafion-Pt contact, as confirmed by the positive shift of the hydrogen underpotential deposition peaks and the very high electrochemical surface area (>100 m^2 g_{Pt}^{-1}) obtained for the Pt NPs. Also, the ability of the hydrophilic BCS surface to potentially facilitate the transport of protons to Pt at low current densities *via* surface water is evidenced by the 100% ECSA obtained during MEA testing, even in environments that are completely free of Nafion. Finally, the oxygen-rich BCS defects also help to anchor the NPs and mitigate agglomeration during accelerated durability testing (ADT).

While mass activities reached 1.3 times the DOE targets, the breakthrough lies in the mechanistic insights obtained, including that proton transport occurs both *via* hydrated BCS surfaces inside the small pores housing the Pt, as well as through Nafion pathways in large pores that contain no Pt, bypassing traditional trade-offs between activity and ionomer coverage. This spatially decoupled approach opens multiple avenues for electrocatalyst design across a range of energy technologies, including in metal–air batteries and during CO_2 reduction, where catalyst hydrophilicity must coexist with overall layer hydrophobicity. The "ball-and-stick" morphology of the BCS is also ideal for flow batteries, where the mesopores generate the required high surface area and the macropores enable unimpeded electrolyte flow. By reimagining the catalyst–ionomer interface, this work provides a representation for enhancing activity and durability simultaneously. Finally, the doctor blade fabrication of the BCS films and the compatibility of ALD with roll-to-roll processing highlight the potential scalability of this catalytic platform for large-scale applications.

Author contributions

M. A., V. I. B., X. L. and S. X. conceived the idea and designed the experiments. In addition, M. A. carried out and optimized the material preparation and characterization. X. L. originally developed the BCS structure and optimized the slurry used in BCS preparation. R. T. and H. N. performed the TPD analyses and interpreted the results. H. Y. carried out the S/TEM analyses of Pt/NCS and Pt/BCS catalyst layers and films. M. K. and M. L. performed microscopic analysis of the Pt/NCS, Pt/BCS, NCS,

and BCS films. Z. W. conducted the Pt ALD on the NCS and BCS substrate. S. X., S. D., and T. G. tested the performance of the ALD-Pt/NCS and ALD-Pt/BCS films in a membrane-electrode assembly in a PEM fuel cell test station. V. I. B., M. A., S. D., F. B. P. and S. X. analyzed the fuel cell data. V. I. B., M. A., and S. X. wrote the overall paper with input from all of the coauthors.

Conflicts of interest

The authors declare no competing interests. The authors have filed a patent related to this work (Marwa Atwa; Shichen Xu; Xiaoan Li; Viola Birss; Friedrich Prinz. Bimodal Nanoporous Carbon Supports for Fuel Cell Applications, PCT/US2023/070645).

Data availability

The data that support the findings of this study are available from the corresponding author upon reasonable request.

Supplementary information includes further experimental results (28 figures and 9 tables). See DOI: **https://doi.org/10.1039/d5ta04830c**.

Acknowledgements

V. I. B. acknowledges the Natural Sciences and Engineering Research Council of Canada (NSERC) as well as the Canada Research Chairs program for financial support. H. N. acknowledges partial support from the JST SICORP grant no. JPMJSC2112. M. A. extends her acknowledgements to the Egyptian Cultural Affairs and Missions Sector and NSERC for scholarship support. We also thank Drs Robert Marriott and Ruohong Sui for their help with the gas sorption measurements and Dr Bin Pan for contact angle measurements. Z. W., S. D., S. X., and F. P. thank the Volkswagen Group of America for financial support and extend their acknowledgments to the Stanford Nano-Shared Facilities (SNSF) where part of the work was performed, supported by the National Science Foundation under award ECCS-1542152. Finally, H. Y., V. I. B., X. L., and M. A. would like to thank Peng Li from the nanoFAB Center at the University of Alberta for his support and for collecting the S/TEM images.

References

1 F. Jiang, C.-Y. Wang and K. S. Chen, *J. Electrochem. Soc.*, 2010, **157**, B342.
2 A. Alaswad, A. Baroutaji, H. Achour, J. Carton, A. Al Makky and A. G. Olabi, *Int. J. Hydrogen Energy*, 2016, **41**, 16499–16508.
3 T. Wilberforce, A. Alaswad, A. Palumbo, M. Dassisti and A. G. Olabi, *Int. J. Hydrogen Energy*, 2016, **41**, 16509–16522.
4 K. Kodama, T. Nagai, A. Kuwaki, R. Jinnouchi and Y. Morimoto, *Nat. Nanotechnol.*, 2021, **16**, 140–147.
5 M. Breitwieser, M. Klingele, S. Vierrath, R. Zengerle and S. Thiele, *Adv. Energy Mater.*, 2018, **8**, 1701257.
6 D. Banham, F. Feng, K. Pei, S. Ye and V. Birss, *J. Mater. Chem. A*, 2013, **1**, 2812.
7 S. Ott, A. Orfanidi, H. Schmies, B. Anke, H. N. Nong, J. Hübner, U. Gernert, M. Gliech, M. Lerch and P. Strasser, *Nat. Mater.*, 2020, **19**, 77–85.
8 Y. Kamitaka, T. Takeshita and Y. Morimoto, *Catalysts*, 2018, **8**, 230.
9 X. X. Wang, Z. H. Tan, M. Zeng and J. N. Wang, *Sci. Rep.*, 2014, **4**, 4437.
10 Z. Zhao, Z. Liu, A. Zhang, X. Yan, W. Xue, B. Peng, H. L. Xin, X. Pan, X. Duan and Y. Huang, *Nat. Nanotechnol.*, 2022, **17**, 968–975.
11 X. Fu, F. M. Hassan, P. Zamani, G. Jiang, D. C. Higgins, J.-Y. Choi, X. Wang, P. Xu, Y. Liu and Z. Chen, *Nano Energy*, 2017, **42**, 249–256.
12 Z. Qiao, C. Wang, Y. Zeng, J. S. Spendelow and G. Wu, *Small*, 2021, **17**, 2006805.
13 K. Kodama, A. Shinohara, N. Hasegawa, K. Shinozaki, R. Jinnouchi, T. Suzuki, T. Hatanaka and Y. Morimoto, *J. Electrochem. Soc.*, 2014, **161**, F649–F652.
14 K. Shinozaki, Y. Morimoto, B. S. Pivovar and S. S. Kocha, *J. Power Sources*, 2016, **325**, 745–751.
15 T. Masuda, F. Sonsudin, P. R. Singh, H. Naohara and K. Uosaki, *J. Phys. Chem. C*, 2013, **117**, 15704–15709.
16 R. Subbaraman, D. Strmcnik, A. P. Paulikas, V. R. Stamenkovic and N. M. Markovic, *ChemPhysChem*, 2010, **11**, 2825–2833.
17 T. Suzuki, K. Kudo and Y. Morimoto, *J. Power Sources*, 2013, **222**, 379–389.
18 M. Wang, J. Zhang, S. Favero, L. J. R. Higgins, H. Luo, I. E. L. Stephens and M. M. Titirici, *Nat. Commun.*, 2024, **15**, 9390.
19 M. J. Dzara, K. Artyushkova, J. Foster, H. Eskandari, Y. Chen, S. A. Mauger, P. Atanassov, K. Karan and S. Pylypenko, *J. Phys. Chem. C*, 2024, **128**, 8467–8482.
20 S. Choi, I. Jang and S. Lee, *Crystals*, 2025, **15**, 129.
21 M. K. Debe, *Nature*, 2012, **486**, 43–51.
22 P. K. Sinha, W. Gu, A. Kongkanand and E. Thompson, *J. Electrochem. Soc.*, 2011, **158**, B831.
23 A. Kongkanand and M. F. Mathias, *J. Phys. Chem. Lett.*, 2016, **7**, 1127–1137.
24 V. Yarlagadda, M. K. Carpenter, T. E. Moylan, R. S. Kukreja, R. Koestner, W. Gu, L. Thompson and A. Kongkanand, *ACS Energy Lett.*, 2018, **3**, 618–621.
25 A. Orfanidi, P. J. Rheinländer, N. Schulte and H. A. Gasteiger, *J. Electrochem. Soc.*, 2018, **165**, F1254–F1263.
26 F. P. Yuqing Guo, W. Chen, Z. Ding, D. Yang, B. Li, P. Ming and C. Zhang, *Electrochem. Energy Rev.*, 2021, **4**, 67–100.
27 S. Kabir, D. J. Myers, N. Kariuki, J. Park, G. Wang, A. Baker, N. Macauley, R. Mukundan, K. L. More and K. C. Neyerlin, *ACS Appl. Mater. Interfaces*, 2019, **11**, 45016–45030.
28 S. M. Dull, S. Xu, T. Goh, D. U. Lee, D. Higgins, M. Orazov, D. M. Koshy, P. E. Vullum, S. Kirsch, G. Huebner, J. Torgersen, T. F. Jaramillo and F. B. Prinz, *Cell Rep. Phys. Sci.*, 2021, **2**, 100297.

29 B. J. O'Neill, D. H. K. Jackson, J. Lee, C. Canlas, P. C. Stair, C. L. Marshall, J. W. Elam, T. F. Kuech, J. A. Dumesic and G. W. Huber, *ACS Catal.*, 2015, **5**, 1804–1825.
30 M. Atwa, X. Li, Z. Wang, S. Dull, S. Xu, X. Tong, R. Tang, H. Nishihara, F. Prinz and V. Birss, *Mater. Horiz.*, 2021, **8**, 2451–2462.
31 B. Pan, C. R. Clarkson, M. Atwa, C. Debuhr, A. Ghanizadeh and V. I. Birss, *J. Colloid Interface Sci.*, 2021, **589**, 411–423.
32 V. Birss, X. Li, D. Banham and D. Y. Kwok, WO pat. 2015135069A1PCT/CA2015/000516, 2015.
33 M. N. Islam, U. Shrivastava, M. Atwa, X. Li, V. Birss and K. Karan, *ACS Appl. Mater. Interfaces*, 2020, **12**, 39215–39226.
34 T. Ishii, S. Kashihara, Y. Hoshikawa, J.-i. Ozaki, N. Kannari, K. Takai, T. Enoki and T. Kyotani, *Carbon*, 2014, **80**, 135–145.
35 S. Rudi, C. Cui, L. Gan and P. Strasser, *Electrocatalysis*, 2014, **5**, 408–418.
36 A. P. G. Arthur and W. Adamson, *Physical Chemistry of Surfaces*, John Wiley & Sons, 6th edn, 1997.
37 L. Zhu, M. Gao, C. K. N. Peh, X. Wang and G. W. Ho, *Adv. Energy Mater.*, 2018, **8**, 1702149.
38 M. Thommes, K. Kaneko, A. V. Neimark, J. P. Olivier, F. Rodriguez-Reinoso, J. Rouquerol and K. S. W. Sing, *Pure Appl. Chem.*, 2015, **87**, 1051–1069.
39 L. L. Kesmodel and G. A. Somorjai, *Phys. Rev. B*, 1975, **11**, 630–637.
40 S. X. Haotian Wang, C. Tsai, Y. Li, C. Liu, J. Zhao, Y. Liu, H. Yuan, F. Abild-Pedersen, F. B. Prinz and Y. C. J. K. Nørskov, *Scieence*, 2016, **354**, 1031–1036.
41 J. Wu and H. Yang, *Acc. Chem. Res.*, 2013, **46**, 1848–1857.
42 G. S. Harzer, A. Orfanidi, H. El-Sayed, P. Madkikar and H. A. Gasteiger, *J. Electrochem. Soc.*, 2018, **165**, F770–F779.
43 M. Prasanna, E. A. Cho, T. H. Lim and I. H. Oh, *Electrochim. Acta*, 2008, **53**, 5434–5441.
44 F. J. Vidal-Iglesias, R. M. Arán-Ais, J. Solla-Gullón, E. Herrero and J. M. Feliu, *ACS Catal.*, 2012, **2**, 901–910.
45 J. Clavilier, R. Faure, G. Guinet and R. Durand, *J. Electroanal. Chem.*, 1980, **107**, 205–209.
46 R. Devivaraprasad, R. Ramesh, N. Naresh, T. Kar, R. K. Singh and M. Neergat, *Langmuir*, 2014, **30**, 8995–9006.
47 J. M. Enrique Herrero, J. M. Feliu and J. Lipkowski, *J. Electroanal. Chem.*, 2002, **534**, 79–89.
48 N. M. Markovic, H. A. Gasteiger and P. N. Ross, *J. Phys. Chem.*, 1995, **99**, 3411–3415.
49 J. Clavilier, *J. Electroanal. Chem.*, 1980, **107**, 211–216.
50 G. A. Kamat, J. A. Zamora Zeledón, G. T. K. K. Gunasooriya, S. M. Dull, J. T. Perryman, J. K. Nørskov, M. B. Stevens and T. F. Jaramillo, *Commun. Chem.*, 2022, **5**, 20.
51 N. Ramaswamy, B. Zulevi, G. McCool, Z. Shi, A. Chavez, D. A. Muller, A. Kongkanand and S. Kumaraguru, *ACS Appl. Eng. Mater.*, 2023, **1**, 2543–2554.
52 D. Zhan, J. Velmurugan and M. V. Mirkin, *J. Am. Chem. Soc.*, 2009, **131**, 14756–14760.
53 J. Liu and I. V. Zenyuk, *Curr. Opin. Electrochem.*, 2018, **12**, 202–208.
54 L. Hu, M. Zhang, S. Komini Babu, A. Kongkanand and S. Litster, *ChemElectroChem*, 2019, **6**, 2659–2666.
55 K. C. a. M. Eikerling, *J. Electrochem. Soc.*, 2011, **158**, B18.
56 L. Xue, Y. Li, X. Liu, Q. Liu, J. Shang, H. Duan, L. Dai and J. Shui, *Nat. Commun.*, 2018, **9**, 3819.
57 M. K. Debe, *J. Electrochem. Soc.*, 2013, **160**, F522–F534.
58 B. Pan, C. R. Clarkson, M. Atwa, X. Tong, C. Debuhr, A. Ghanizadeh and V. I. Birss, *Transp. Porous Media*, 2021, **137**, 555–574.
59 R. Tang, K. Taguchi, H. Nishihara, T. Ishii, E. Morallón, D. Cazorla-Amorós, T. Asada, N. Kobayashi, Y. Muramatsu and T. Kyotani, *J. Mater. Chem. A*, 2019, **7**, 7480–7488.
60 Q. Wang, M. Eikerling, D. Song and Z. Liu, *J. Electroanal. Chem.*, 2004, **573**, 61–69.
61 A. Ohma, K. Shinohara, A. Iiyama, T. Yoshida and A. Daimaru, *ECS Trans.*, 2011, **41**, 775–784.
62 X. Yu and S. Ye, *J. Power Sources*, 2007, **172**, 145–154.

